# Online Attribute Matching Based Few-Sample Data-Driven Diagnosis of Electrical Faults in PMSM Drive

Luhan Jin, *Graduate Student Member, IEEE*, Xueqing Wang, *Member, IEEE*, Yao Mao, *Member, IEEE*, Linlin Lu, *Student Member, IEEE*, and Zheng Wang, *Senior Member, IEEE*

***Abstract*—In this article, an online attribute matching based few-sample data-driven diagnosis method for electrical faults in permanent magnet synchronous motor drive is proposed to improve the diagnosis precision with fewer training data and lower computational complexity. By incorporating the motor model knowledge in the feature extraction process, effective and robust input features can be extracted without consuming large computing resources. Instead of directly predicting the fault mode in the original huge solution space, an integrated attribute learner is specifically designed to predict the fault attributes in the simplified solution space to reduce both network size and required training data. Finally, based on the look-up table for the fault attribute vector, an attribute matching strategy is proposed to determine the specific fault mode with the consideration of unknown faults. Comprehensive experiments verify that the proposed method can identify each fault mode efficiently with an average diagnostic accuracy of 99.12% and the computational time of 0.1 ms, which outperforms the existing data-driven diagnosis methods for motor drives.**

***Index Terms*—Attribute matching, data-driven diagnosis, electrical faults, fault diagnosis, integrated attribute learner, permanent magnet synchronous motor (PMSM) drive.**

## I. INTRODUCTION

PERMANENT magnet synchronous motor (PMSM) has been widely applied in various industrial applications due to its high-power density and high efficiency [1], [2], [3], [4]. Due to aging, overloading, and abnormal operations, the PMSM drive is prone to various failures. The faults that occurred in the PMSM drive may result in catastrophic damages to the overall system through fault propagation. Therefore, fault diagnosis of PMSM drive is extremely necessary.

The faults of PMSM drive can be mainly divided into three types, namely mechanical fault, electrical fault, and magnetic fault. Among them, open-phase fault (OPF) and open-switch fault (OSF) are two common electrical faults [5], [6], [7]. Normally, OPF and OSF do not cause the shutdown of motor drive immediately but bring about serious torque ripples as well as considerable mechanical vibration which may lead to the whole system collapse through fault propagation [8]. Thus, this article focuses on fault diagnosis of both OPF and OSF in PMSM drive.

In general, the fault diagnosis methods for OPF and OSF in motor drive can be categorized into model-based, signal-based, and data-based methods [9]. The model-based method usually requires accurate system models to monitor the residuals between the measured output and model-predicted output, which are typically built based on the machine model principles [10], [11], [12], observer-based approaches [13], [14], [15], and state or parameter estimation techniques [16], [17], [18]. However, model-based methods usually suffer from the impact of unmodeled characteristics and parameter variations, which cannot be ignored in practical applications. On the other hand, the signal-based method employs the measured signals to construct fault indicators without the requirement of machine models. Since the OPF and OSF will cause different distortions in current and voltage signals, the signal-based methods can be subdivided into current-based approaches [19], [20], [21] and voltage-based approaches [22], [23], [24]. The current-based approaches have been extensively studied since they are independent of machine parameters and do not require additional sensors. However, these approaches usually take one fundamental period to collect enough current information, which will prolong the diagnostic time. By contrast, the voltage-based methods can achieve fast diagnosis and have higher immunity to false alarms. However, additional sensors are needed to acquire real-time voltage signals, which will increase the system cost.

Apart from the model-based and signal-based methods, the data-based method gradually becomes a promising solution for fault diagnosis with the advancement of artificial intelligence.

---

Manuscript received 26 June 2023; revised 10 September 2023; accepted 17 November 2023. Date of publication 28 November 2023; date of current version 22 December 2023. This work was supported in part by National Natural Science Foundation of China under Grant 62303333 and in part by Science and Technology Projects of Chengdu City under Grant 2022-YF05-00228-SN. Recommended for publication by Associate Editor D. Xu. *(Corresponding authors: Xueqing Wang; Yao Mao.)*

Luhan Jin, Yao Mao, and Linlin Lu are with the National Key Laboratory of Optical Field Manipulation Science and Technology, Chinese Academy of Sciences, Chengdu 610209, China, also with the Key Laboratory of Optical Engineering, Chinese Academy of Sciences, Chengdu 610209, China, also with the Institute of Optics and Electronics, Chinese Academy of Sciences, Chengdu 610209, China, and also with the University of Chinese Academy of Sciences, Beijing 101408, China (e-mail: jinluhan21@mails.ucas.ac.cn; maoyao@ioe.ac.cn; lulinlin21@mails.ucas.ac.cn).

Xueqing Wang is with the College of Electrical Engineering, Sichuan University, Chengdu 610065, China (e-mail: xwang@scu.edu.cn).

Zheng Wang is with the School of Electrical Engineering, Southeast University, Nanjing 210096, China (e-mail: zwang@eee.hku.hk).

Color versions of one or more figures in this article are available at https://doi.org/10.1109/TPEL.2023.3335268.

Digital Object Identifier 10.1109/TPEL.2023.3335268

As its name implies, the data-based method normally requires a large volume of data to extract the mapping relationship between the network input and fault mode without knowing the system model or signal patterns [25]. Thus, the data-based method is more robust against parameter variations and suitable for applications in various systems, compared with model-based and signal-based methods. To simultaneously improve diagnostic accuracy and efficiency, literature [26] proposes a fault diagnosis strategy for open-circuit fault in a cascaded H-bridge multilevel inverter system based on the principal component analysis (PCA) and multiclass relevance vector machine. Aiming to solve the uncertainty problem in fault diagnosis of inverters, a PCA and Bayesian network-based method is proposed in [27] with the spectrums of two line-to-line voltages adopted as feature indicators. To increase the learning diversity and achieve fast diagnosis, a data-driven method based on hybrid ensemble learning and sliding-window classification is proposed in [9] to identify the open-circuit fault in motor drive system. In detail, the extreme learning machine (ELM) and random vector functional link (RVFL) network are fused as an ensemble classifier in [9] to learn the mapping relationship between the input feature and fault modes. The RVFL network is also used in [28] to achieve the simultaneous diagnosis of open-circuit and current sensor fault with an overall accuracy of 98.83%. Unfortunately, when it comes to practical applications, the above data-based methods are not suitable due to the requirement of a large-scale neural network and the huge amount of experimental data. The calculation of a large-scale network will cause heavy computation burden to the controller and the massive acquisition of experimental data will lead to the irreversible damage to the practical system. Besides, the capability of detecting unknown faults is a critical concern. The unknown faults refer to the possible failures that are ignored by the fault diagnosis methods. Without considering unknown faults in the diagnosis schemes, the faults will be neglected or misdiagnosed, which will induce false disposal and cause further damages to the system. Thus, the detection of unknown faults is essential for the diagnosis methods to identify abnormal states timely and avoid further damages.

Based on the above literature review, it is still challenging to establish an efficient online data-driven diagnosis approach for electrical faults in motor drives with limited experimental data, which is essential in practical applications. To this end, an attribute matching based data-driven method is proposed in this article for few-sample electrical fault diagnosis of PMSM drive. With the proposed data-driven method, online fault diagnosis of each fault mode can be easily fulfilled with lower computational burden and misdiagnosis can be effectively avoided. Additionally, the proposed data-driven method has been implemented in the common digital signal processor (DSP) to verify its practicality. The main innovations and contributions of the proposed method can be summarized as follows.

1) Without involving sophisticated feature extraction algorithms, the proposed method extracts the combination of torque and electrical angle as the input features by utilizing motor model knowledge in the feature extraction process. Theoretical derivation of torque fluctuation equations guarantees the stable patterns and uniqueness of the extracted features, which is conducive to improving the diagnostic performance. Furthermore, only few simple algebraic operations are required to calculate the extracted features in the proposed method, promoting the reduction of online computational burden.
2) By introducing noticeable attributes to describe each fault mode, the proposed method transforms the original multiclassification problem of fault modes into simple binary classification problems of fault attributes. Compared with most conventional data-driven diagnosis methods for motor drives which directly predict the fault mode with enormous neural networks in the original huge solution space, the proposed method can achieve accurate fault diagnosis using smaller neural networks and fewer training data due to the reduction of solution space.
3) Without considering the unknown faults, misdiagnosis may easily occur in the existing methods, leading to false alarms and further damages. To improve the diagnosis precision, an attribute matching strategy is proposed to determine the specific fault mode with the consideration of unknown faults. By comparing the predicted fault attribute vector of the present sample with target fault attribute vectors in the lookup table, the unknown fault can be effectively indicated in the proposed method to avoid misdiagnosis.

The rest of this article is organized as follows. Section II describes the modeling of PMSM and fault analysis. In Section III, the general fault diagnosis framework of the proposed method is briefly summarized, and the corresponding details are discussed in each subsection. Experimental results are given in Section IV to show the online practicality and superiority of the proposed method. Finally, Section V concludes this article.

## II. MACHINE MODELING AND FAULT ANALYSIS

### A. PMSM Model

The voltage equations of PMSM in the synchronous rotating coordinate system are given as

$$\begin{cases} u_d = R_s i_d + L_d \frac{di_d}{dt} - \omega_r L_q i_q \\ u_q = R_s i_q + L_q \frac{di_q}{dt} + \omega_r L_d i_d + \omega_r \psi_f \end{cases} \tag{1}$$

where $R_s$ is the stator resistance, $L_d$ and $L_q$ are the $d$-axis, $q$-axis inductance, respectively. $\omega_r$ is the rotor electrical velocity and $\psi_f$ is the amplitude of rotor flux.

The electromagnetic torque of PMSM can be expressed as

$$T_e = \frac{3}{2} N_p \left[ \psi_f i_q + (L_d - L_q) i_d i_q \right] \tag{2}$$

where $N_p$ represents the pole pair number.

### B. OPF and OSF Analysis

Without loss of generality, Phase-A fault is taken as an example in the following analysis. The impacts of phase-A OPF and OSF are illustrated in Fig. 1. In the Fig. 1(a), the phase-A current paths of different switching states and current directions

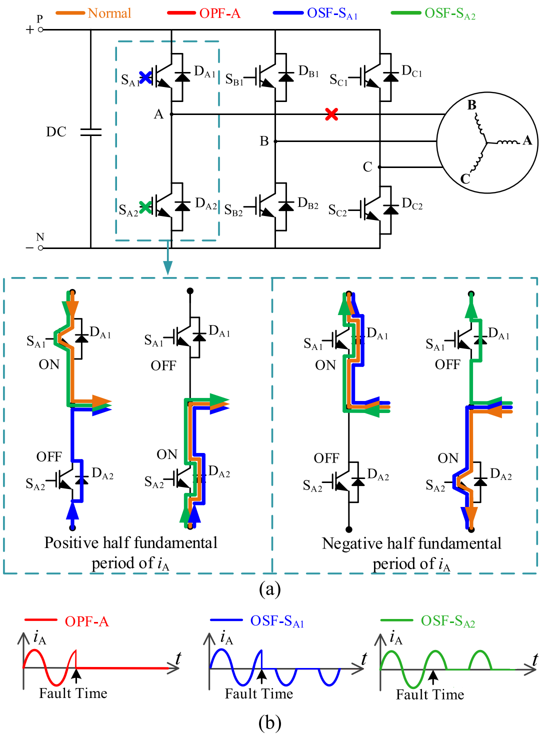

Fig. 1. Impacts of Phase-A OPF and OSF in PMSM drive. (a) Current paths of different operating states. (b) Current waveforms.

in normal operation are marked with orange. The occurrence of phase-A OPF (OPF-A) will block the faulty phase-A current $i_{\mathrm{A}}$, as illustrated with the red mark in Fig. 1(a). As a result, the faulty phase-A current $i_{\mathrm{A}}$ will be forced to zero consistently during the whole fundamental period, as shown with the red curve in Fig. 1(b). When the OSF in the upper switch $\mathrm{S_{A1}}$ (OSF-$\mathrm{S_{A1}}$) occurs, the original current path outflowing through the upper switch $S_{\mathrm{A1}}$ will be blocked and the faulty phase-A current $i_{\mathrm{A}}$ in the positive half fundamental period can only outflow through the lower diode $D_{\mathrm{A2}}$ instead, as shown with the blue current path in Fig. 1(a). The change of current path in this case will force the high level of the faulty inverter leg to low level, which will make the positive current $i_{\mathrm{A}}$ to decrease until zero [30]. Since the faulty phase-A current path of OSF-$\mathrm{S_{A1}}$ in other operating states do not flow through the faulty switch $\mathrm{S_{A1}}$, they are the same as those in normal operation. Based on the above analysis, the faulty phase-A current $i_{\mathrm{A}}$ under OSF-$\mathrm{S_{A1}}$ will remain zero in the positive half fundamental period and return to the normal sinusoidal current patterns rapidly once it enters the negative half fundamental period, as shown with the blue curve in Fig. 1(b). Similarly, when the OSF in the lower switch $S_{\mathrm{A2}}$ (OSF-$\mathrm{S_{A2}}$) occurs, the original current path inflowing through the lower switch $S_{\mathrm{A2}}$ is blocked and the faulty phase-A current $i_{\mathrm{A}}$ during the negative half fundamental period can only inflow through the upper diode $\mathrm{D_{A1}}$ while the faulty phase-A current path under OSF-$\mathrm{S_{A2}}$ in other operating states are not affected, as shown with the green current path in Fig. 1(a). Thus, the faulty current $i_{\mathrm{A}}$ will remain zero until it enters the positive half fundamental period, as shown with the green curve in Fig. 1(b).

To differentiate the positive and negative half fundamental periods of phase currents, the relationship between normal phase current references and rotor electrical angle $\theta_e$ should be derived first. According to the inverse Park transformation, the normal phase current references can be expressed as

$$\begin{cases} i^*_{\mathrm{A-Normal}} = -i_q^* \sin(\theta_e) \\ i^*_{\mathrm{B-Normal}} = -i_q^* \sin\left(\theta_e - \frac{2}{3}\pi\right) \\ i^*_{\mathrm{C-Normal}} = -i_q^* \sin\left(\theta_e + \frac{2}{3}\pi\right) \end{cases}. \tag{3}$$

By combining (3) and the analysis of fault features, the faulty phase currents in the whole fundamental period under phase-A OPF and OSF can be expressed as

$$\begin{cases} i_{\mathrm{A-OPF-A}} \approx 0 \\ i_{\mathrm{A-OSF-S_{A1}}} \approx \begin{cases} -i_q^* \sin(\theta_e)\ (\theta_e \in [0,\pi]) \\ 0\ (\theta_e \in [\pi, 2\pi]) \end{cases} \\ i_{\mathrm{A-OSF-S_{A2}}} \approx \begin{cases} 0\ (\theta_e \in [0,\pi]) \\ -i_q^* \sin(\theta_e)\ (\theta_e \in [\pi, 2\pi]) \end{cases} \end{cases}. \tag{4}$$

### C. Torque Fluctuation Analysis

Unlike most data-based diagnosis methods which use the spectrums of three-phase currents or line-to-line voltages as the input to the neural network, the combination of torque $T_e$ and electrical angle $\theta_e$ are employed as the network input in this article to reduce the network size and reserve the complete faulty information. Compared with the spectrums of three-phase currents or line-to-line voltages, the torque $T_e$ can be directly obtained through simple calculations without consuming large computing resources.

Since the OPF and OSF can cause different current distortions in the PMSM drive, the torque fluctuations will be accordingly produced. To simplify the analysis, the surface-mounted PMSM will be analyzed as an example while the interior PMSM shares the same conclusion.

By combining Park transformation and basic current constraints under OPF-A, the currents on the $d$-$q$ axis can be expressed as

$$\begin{cases} i_d = \frac{2\sqrt{3}}{3} i_B \sin(\theta_e) \\ i_q = \frac{2\sqrt{3}}{3} i_B \cos(\theta_e) \end{cases}. \tag{5}$$

Neglecting the high-order harmonic components, the phase-B current $i_B$ under OPF-A can be expressed as

$$i_B \approx K \times \sin(\theta_e + \theta_B) \tag{6}$$

where $K$ is the current coefficient, determining the amplitude of $i_B$. $\theta_B$ is the initial phase angle of $i_B$.

Owing to the change of machine model after OPF-A, the $d$–$q$ axis currents can hardly track their original references and current fluctuations will be accordingly generated. However, the closed-loop control for $d$–$q$ axis currents will automatically make the average value of $d$–$q$ axis currents tend to their references (0 for $i_d$, $i_q{}^*$ for $i_q$). According to (5), $i_{\mathrm{B}}$ should be orthogonal to $\sin(\theta_e)$ to simultaneously satisfy the average $d$-axis current of 0 and the average $q$-axis current of $i_q{}^*$. In other words, $\theta_B$ is almost equal to $\pi/2$ under the closed-loop control for $d$–$q$ axis currents under OPF-A. Applying the above

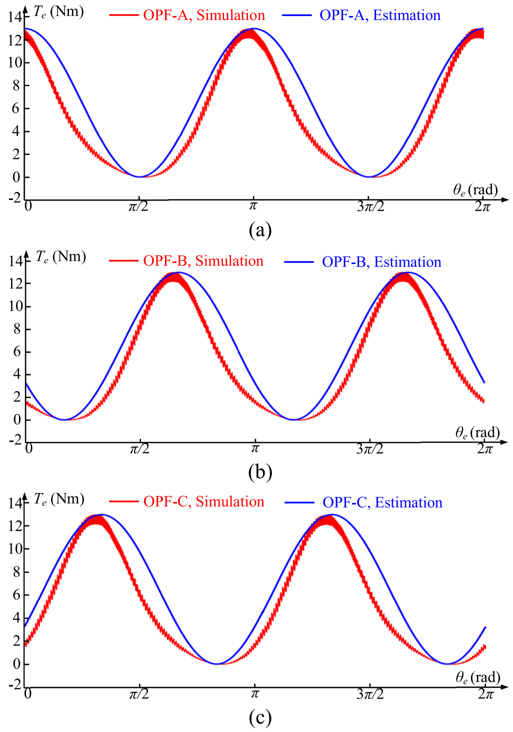

(a)

(b)

(c)

Fig. 2. Simulated and estimated torques under different OPFs of PMSM drive. (a) OPF-A. (b) OPF-B. (c) OPF-C.

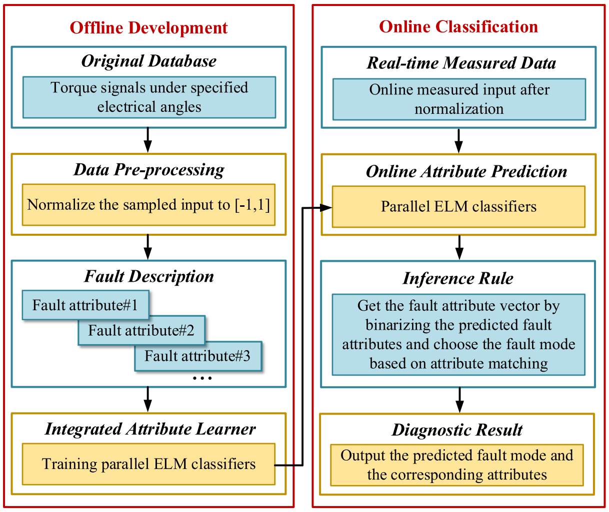

Fig. 3. Proposed fault diagnosis framework.

constraint on $q$-axis current $i_q$, the current coefficient $K$ can be further calculated as follows:

$$K \approx \frac{\sqrt{3}\pi i_q^*}{\int_0^{2\pi} \cos^2(\theta_e) d\theta_e} = \sqrt{3} i_q^*. \tag{7}$$

Based on the above analysis, the phase-B current $i_B$ can be further expressed as

$$i_B \approx \sqrt{3} i_q^* \cos(\theta_e). \tag{8}$$

According to (2), (5), and (8), the torque $T_e$ under OPF-A can be further expressed with electrical angle $\theta_e$, as shown in

$$T_{e\_\mathrm{OPF-A}} \approx 3 N_p \psi_f i_q^* \cos^2(\theta_e). \tag{9}$$

The torque fluctuation equations under OPF in other phases can be derived in the same way. To prove the correctness of the above theoretical derivation, the torque waveforms obtained through simulation and estimation under different OPFs are compared in Fig. 2. In Fig. 2, the simulated torques and estimated torques under OPFs in arbitrary phases have similar waveform patterns, which verify the correctness of above theoretical derivation. Besides, it can be concluded from Fig. 2 that the combination of torque $T_e$ and electrical angle $\theta_e$ under different OPFs have distinguishable diversities that can be used to conduct fault classification. The above conclusion applies equally to the OSFs. As analyzed in Section II-B, since phase-A OSF will only cause zero phase-A current in the positive or negative half fundamental period, the torque fluctuations under phase-A OSF will follow the same pattern as OPF-A only in the faulty half fundamental period. In the healthy half fundamental period, the output torque in phase-A OSFs remains stable. In a word, the fault diagnosis for both OPF and OSF can be fulfilled by combining the electrical angle $\theta_e$ and the corresponding torque $T_e$ as the network input.

## III. Fault Diagnosis Methodology

In a practical system, massive acquisition of experimental data under various faults can easily cause irreversible damage to the system. However, most of the existing data-based methods are conducted based on the premise of sufficient experimental data. To fulfill the few-sample diagnosis, a novel data-driven fault diagnosis method is proposed in this article based on attribute matching and a randomized learning technique named ELM. The effectiveness of the few-sample diagnosis in the proposed method can be ensured owing to the following two points. First, by utilizing the model knowledge in faulty operation, the torque fluctuation equations under both OPF and OSF are theoretically derived and the combination of torque and electrical angle are extracted as the input features in the proposed method. The theoretical analysis in Section II-C proves that the extracted features under different fault modes have stable patterns and distinguishable differences, which reduces the difficulty of training the attribute learner. As a result, the required training samples can be accordingly reduced. Second, the use of attribute learner can simplify the original complex multi-classification problem of fault modes as binary classification problems of fault attributes. Owing to the reduction of searching space, both the model complexity of the attribute learner and the required training samples can be effectively reduced. The general framework of the proposed method is shown in Fig. 3. It consists of offline model training and online diagnostic process.

During the offline model training, the proposed method only needs a small amount of experimental data, i.e., the sampled torques $T_e$ under specified electrical angles. For the data preprocessing part, the collected data is normalized to the interval $[-1,1]$ to facilitate the model training stage. Unlike existing data-based diagnosis methods, noticeable fault attributes are provided to describe each fault in the proposed fault diagnosis scheme. After that, parallel ELM classifiers are trained to constitute an integrated attribute learner, which can extract the mapping relationship between the network input and the corresponding fault attributes. For online diagnostic process, the real-time normalized torque signals under specified electrical angles are imported to the pre-trained parallel ELM classifiers to predict fault attributes of the present sample. The fault attribute vector of the present sample can be obtained by binarizing the predicted fault attributes. Finally, the fault mode is determined based on attribute matching.

### A. Data Selection and Pre-Processing

Based on the detailed analysis in Section II, the torques $T_e$ at the angles of 0, $\pi/3$, $2\pi/3$, $\pi$, $4\pi/3$, and $5\pi/3$ are selected as the input to the attribute learner. It can be found from Fig. 2 that the combination of torque signals and electrical angles have distinguishable fault features. Thus, different OPFs and OSFs can be easily distinguished with torque $T_e$ under specified angles as the network input. By analyzing the electrical characteristics of PMSM drive in faulty operation, the proposed method can diagnose OPFs and OSFs using fewer data dimensions. Compared with existing data-based diagnosis methods which adopt the spectrums of three-phase currents or line-to-line voltages as the network input, the proposed method uses variables that can be easily obtained without consuming large computing resources.

For data pre-processing, linear normalization is adopted to normalize the sampled input to the interval [−1,1] to facilitate the model training stage. A set of sampled data $\boldsymbol{x}$ can be expressed in the form of column vector as follows:

$$\boldsymbol{x} = \left[T_e(0), T_e\left(\frac{\pi}{3}\right), T_e\left(\frac{2\pi}{3}\right), T_e(\pi), T_e\left(\frac{4\pi}{3}\right), T_e\left(\frac{5\pi}{3}\right)\right]^T \tag{10}$$

where the superscript $T$ represents the transpose of the matrix.

By applying linear normalization [31], the normalized input $\boldsymbol{x}_n$ can be expressed as follows:

$$\boldsymbol{x}_n = -1 + 2\frac{\boldsymbol{x} - \min(\boldsymbol{x})}{\max(\boldsymbol{x}) - \min(\boldsymbol{x})}. \tag{11}$$

For data-driven diagnosis methods, the quality of the input data can directly influence the diagnosis performance. In this article, the high signal-to-noise ratio characteristic of the input features can be guaranteed by the following three points. First, the extracted input features in the proposed method, i.e., the combination of torque and electrical angle, have been theoretically proved to possess the stable patterns and distinguishable differences under different fault modes. Second, the torque in the extracted features is calculated with motor currents. The high-frequency noise in motor currents will be automatically filtered by the motor inductance, which enhances the quality of the input features in the proposed method. Finally, the current sensor used in this article (LEM LA25-NP) can achieve a low sampling error of 0.5%, which also contributes to the high signal-to-noise ratio of the input features. In the aspect of outliers, the motor currents are unable to change abruptly due to the existence of motor inductance. Thus, the large current variation at the adjacent sampling time indicates that an outlier has occurred. In this article, the double sampling technique is employed to avoid the use of outliers.

TABLE I
DEFINED FAULT ATTRIBUTES FOR OPF AND OSF

| No. | Attribute |
|---|---|
| Attribute #1 | Fault occurs in Phase-A |
| Attribute #2 | Fault occurs in Phase-B |
| Attribute #3 | Fault occurs in Phase-C |
| Attribute #4 | Faulty phase current keeps zero in the whole cycle |
| Attribute #5 | Faulty phase current keeps zero only in the positive part |
| Attribute #6 | Faulty phase current keeps zero only in the negative part |

### B. Integrated Attribute Learner

The existing data-based diagnosis methods will consume massive experimental data and computing resources by using a large-size neural network to directly predict the fault mode, which is not suitable for practical applications. By comparison, the proposed method provides noticeable fault attributes to describe each fault and attribute learners are developed to extract the mapping relationship between the network input and fault attributes. In this way, the original complex multiclassification problem of fault modes is transformed into few simple binary classification problems of fault attributes. Thus, both network scale and required training data can be effectively reduced due to the reduction of searching space. Based on above, the performance of the proposed method is directly related to the selection of fault attributes. The rules of selecting effective attributes can be condensed as follows: First, the selected attributes need to reflect the real state of the fault. Second, any studied fault mode can be uniquely determined by using the selected attributes. Finally, the number of selected attributes should be as small as possible to reduce the computational complexity of the integrated attribute learner. For the diagnosis of single OPF and OSF in PMSM drive, there are nine kinds of fault possibilities. Based on the system analysis in faulty operation, six fault attributes regarding the fault location and fault category information are defined, as given in Table I. The extracted fault location and fault category information from the fault attributes can jointly distinguish the specific fault mode.

According to Table I, the fault attribute vector for each fault mode can be obtained, as shown in Fig. 4. Taking OPF-A as an example, the phase-A current $i_A$ will keep zero after the fault occurs. Thus, the fault attribute vector for OPF-A is [1 00 1 00], as shown in the first row of Fig. 4.

Next, six small-scale ELMs are developed in parallel to constitute an integrated attribute learner to predict fault attributes. The ELM is originally proposed in [29] based on the single hidden-layer feedforward neural network (SLFN). The essence of ELM is to randomly choose the input weights and hidden biases while the output weights are analytically determined

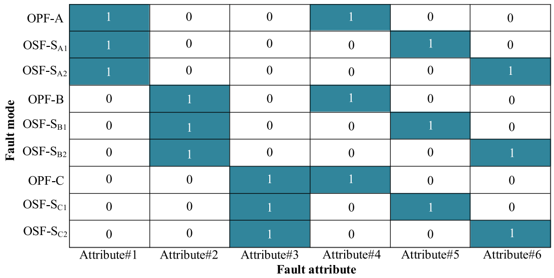

| Fault mode | Attribute#1 | Attribute#2 | Attribute#3 | Attribute#4 | Attribute#5 | Attribute#6 |
|---|---|---|---|---|---|---|
| OPF-A | 1 | 0 | 0 | 1 | 0 | 0 |
| OSF-S$_{A1}$ | 1 | 0 | 0 | 0 | 1 | 0 |
| OSF-S$_{A2}$ | 1 | 0 | 0 | 0 | 0 | 1 |
| OPF-B | 0 | 1 | 0 | 1 | 0 | 0 |
| OSF-S$_{B1}$ | 0 | 1 | 0 | 0 | 1 | 0 |
| OSF-S$_{B2}$ | 0 | 1 | 0 | 0 | 0 | 1 |
| OPF-C | 0 | 0 | 1 | 1 | 0 | 0 |
| OSF-S$_{C1}$ | 0 | 0 | 1 | 0 | 1 | 0 |
| OSF-S$_{C2}$ | 0 | 0 | 1 | 0 | 0 | 1 |

Fault attribute

Fig. 4. Fault attribute matrix for different OPFs and OSFs.

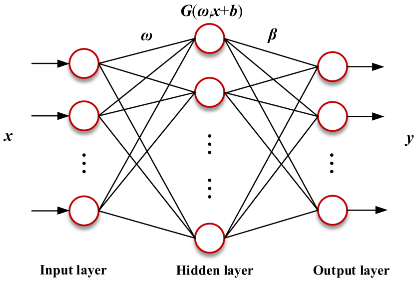

Fig. 5. Architecture of ELM.

using Moore-Penrose generalized inverse method or other optimization methods. It has been found in [32] that random search over input to the hidden layer is much more computationally efficient than tuning all the network parameters in SLFN. Thus, ELM has both fast learning speed and less computational burden compared with other neural networks. The ELM has been successfully adopted in various fields with satisfactory performance due to its simplicity, fast learning speed, and good generalization performance [33], [34], [35]. Thus, it is selected as one of the alternative attribute learners in this article to verify the effectiveness of the proposed fault diagnosis framework. Other high-performance neural networks, such as Bayesian network and convolutional neural network, can also be adopted as candidate attribute learners in the proposed diagnosis framework. The typical architecture of ELM is plotted in Fig. 5.

Assume $Z_N = \{(\boldsymbol{x}_i, \boldsymbol{y}_i) | \boldsymbol{x}_i \in \mathbf{R}^{\mathrm{n}}, \boldsymbol{y}_i \in \mathbf{R}^{\mathrm{m}}\}^N{}_{i=1}$ constitutes a training data set, where $\boldsymbol{x}_i$ is a $n\times 1$ input vector and $\boldsymbol{y}_i$ is a $m\times 1$ target vector. Under the assumption of zero approximation error, the output function of ELM can be written as follows:

$$f(\boldsymbol{x}_i) = \sum_{j=1}^{L} \boldsymbol{\beta}_j \cdot G(\boldsymbol{\omega}_j^T \cdot \boldsymbol{x}_i + b_j) = \boldsymbol{y}_i, i = 1, 2, \ldots, N \tag{12}$$

where $\omega_j$ is the weight vector between the input layer and the $j$th hidden node, $b_j$ is the bias of the $j$th hidden node, $G$ refers to the activation function, $\beta_j$ refers to the weight vector between the $j$th hidden node and output layer, and $L$ represents the number of hidden nodes.

For simplicity, (12) can be rewritten compactly as follows:

$$\mathbf{H}\boldsymbol{\beta} = \mathbf{Y} \tag{13}$$

where the output weight matrix $\beta = [\beta_1\ \beta_2\ \ldots\ \beta_L]^T{}_{L\times m}$, the training target matrix $\mathbf{Y} = [\boldsymbol{y}_1\ \boldsymbol{y}_2\ \ldots\ \boldsymbol{y}_N]^T{}_{N\times m}$, and the hidden layer output matrix $\mathbf{H}$ can be expressed as follows:

$$\mathbf{H} = \begin{bmatrix} G(\boldsymbol{\omega}_1 \cdot \boldsymbol{x}_1 + b_1) & \cdots & G(\boldsymbol{\omega}_L \cdot \boldsymbol{x}_1 + b_L) \\ \vdots & \cdots & \vdots \\ G(\boldsymbol{\omega}_1 \cdot \boldsymbol{x}_N + b_1) & \cdots & G(\boldsymbol{\omega}_L \cdot \boldsymbol{x}_N + b_L) \end{bmatrix}_{N\times L} = \begin{bmatrix} \mathbf{h}(\boldsymbol{x}_1) \\ \vdots \\ \mathbf{h}(\boldsymbol{x}_N) \end{bmatrix}. \tag{14}$$

Using the Moore-Penrose generalized inverse, the optimal output weight matrix $\beta^*$ can be calculated as follows:

$$\boldsymbol{\beta}^* = \mathbf{H}^\dagger \mathbf{Y} \tag{15}$$

where $\mathbf{H}^\dagger$ is the Moore-Penrose generalized inverse of $\mathbf{H}$.

Due to the randomized mechanism of ELM, each parallel ELM classifier shares the same structure from input layer to hidden layer, which further reduces the computational complexity of the integrated attribute learner. The training process of the integrated attribute learner can be summarized as follows: Initialize the input weight matrix $\omega$; calculate the hidden layer matrix $\mathbf{H}$; and calculate the optimal output weight matrix $\beta^*$ for each parallel ELM based on (15). The Moore-Penrose generalized inverse $\mathbf{H}^\dagger$ in (15) is calculated using the orthogonal projection method in

$$\mathbf{H}^\dagger = \begin{cases} \left(\mathbf{H}^T\mathbf{H}\right)^{-1}\mathbf{H}^T, & \mathbf{H}^T\mathbf{H} \text{ is nonsingular} \\ \mathbf{H}^T\left(\mathbf{H}\mathbf{H}^T\right)^{-1}, & \mathbf{H}\mathbf{H}^T \text{ is nonsingular} \end{cases}. \tag{16}$$

To alleviate the overfitting problem, a small positive hyperparameter $\alpha$ is added to the diagonal elements of matrix $\mathbf{H}^T\mathbf{H}$ or $\mathbf{H}\mathbf{H}^T$ based on the ridge regression theory [36]. Thus, the optimal output weight matrix $\beta^*$ can be finally derived as

$$\boldsymbol{\beta}^* = \begin{cases} \left(\alpha\mathbf{I}_L + \mathbf{H}^T\mathbf{H}\right)^{-1}\mathbf{H}^T\mathbf{Y}, & \mathbf{H}^T\mathbf{H} \text{ is nonsingular} \\ \mathbf{H}^{\mathrm{T}}\left(\alpha\mathbf{I}_N + \mathbf{H}\mathbf{H}^T\right)^{-1}\mathbf{Y}, & \mathbf{H}\mathbf{H}^T \text{ is nonsingular} \end{cases} \tag{17}$$

where $\mathbf{I}_L$ and $\mathbf{I}_N$ are the $L\times L$ and $N\times N$ identity matrices, respectively. The use of hyperparameter $\alpha$ can limit the searching space of output weight matrix $\beta$, which will enhance the robustness against various noises and contribute to better generalization performance for the integrated attribute learner.

### *C. Attribute Matching-Based Fault Classification*

Due to the calculation error produced in the training process of ELM, the predicted fault attributes may not be exactly integer 0 or 1. Thus, the output of each parallel ELM classifier is binarized based on a well-designed threshold $f_{th}$, which can be expressed as follows:

$$f_{i-b} = \begin{cases} 1, & f_i \geq f_{th} \\ 0, & \text{otherwise} \end{cases} \tag{18}$$

where $f_i$ is the output of $i$th parallel ELM classifier and $f_{i\text{-}b}$ is the corresponding binarized output.

After binarization process, the predicted six fault attributes are transformed into a binarized attribute vector and fault mode is determined based on attribute matching. Different from the

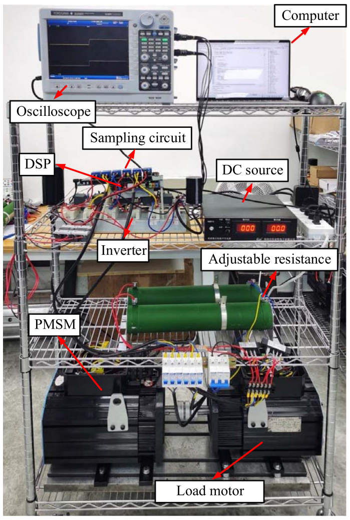

Fig. 6. Experimental platform.

existing data-based diagnosis methods, the proposed method is able to detect unknown faults, which is critical to practical applications. Existing data-based diagnosis methods will always predict the fault mode from a limited number of candidate fault modes. However, the number of potential fault types will significantly increase in practical applications. When unknown faults happen, misdiagnosis will occur in these methods without doubt. By comparison, the proposed method will determine the fault mode only if the predicted fault attribute vector of the present sample is consistent with a target fault attribute vector in Fig. 4. When an unknown fault occurs, the predicted fault attribute vector will not match any target fault attribute vectors of candidate fault modes. Under this circumstance, the proposed method will output the “unknown fault” sign.

## IV. Experimental Validation

The proposed data-driven fault diagnosis method is verified on a laboratory prototype of two-level VSI-fed three-phase PMSM drive. The developed experimental platform is shown in Fig. 6. In the experiment, the DSP (TMS320F28335) is employed as the main controller to obtain sampling signals, perform the control strategy, and generate the desired pulsedwidth modulation pulses for the inverters. Three IGBT half-bridge modules (SKM75GB12T4) are used to supply the PMSM. The current sensors (LEM LA25-NP) and voltage sensor (LEM LV25-P) constitute the sampling circuit, which are used to measure the phase currents and the dc-link voltage with the sampling error of 0.5% and 0.9%, respectively. In addition, the adjustable resistance is connected to the load motor to change the load torque. For the convenience of data acquisition and visualization, the oscilloscope (DL850EV) is used to collect the training data samples and visualize the online diagnostic results. The key parameters of the experimental platforms are given in Table II. Since the input features of different fault modes in the proposed method, namely the combination of torque and electrical angle, have stable patterns and distinct differences in any control frameworks, the proposed method is generally applicable to any control frameworks of PMSM. In this article, the typical vector control is adopted in the experiment as one of the alternative control frameworks to prove the feasibility of the proposed data-driven fault diagnosis method.

TABLE II
Parameters of Experimental Platform

| *Name* | *Value* |
|---|---|
| Pole pair number | 4 |
| *d*-axis inductance | 8.91 mH |
| *q*-axis inductance | 17.03 mH |
| PM flux | 0.3 Wb |
| Stator resistance | 1.4 Ω |
| Switching frequency | 5 kHz |

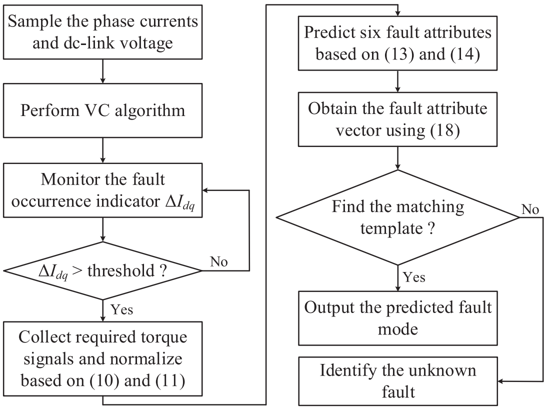

Fig. 7. Flowchart of online diagnosis using DSP.

For ease of understanding, the implementation flowchart of online diagnosis using DSP is shown in Fig. 7. The fault diagnosis process will be enabled when the *d*–*q* axis current tracking error $\Delta I_{dq}$ becomes larger than a preset threshold. Then, the torque signals under specific electrical angles are calculated and normalized within one fundamental period based on (10) and (11). By utilizing predicting (13) and (14), six fault attributes of the present sample can be predicted and the binarized fault attribute vector is accordingly obtained using (18). The final step of the proposed data-driven diagnosis method is to find the matching template for the predicted fault attribute vector to identify the specific fault mode. If no template matches with the predicted fault attribute vector, the unknown fault will be identified.

### A. *Data Collection and Model Building*

To perform the proposed fault diagnosis method, a data set is first collected to train six parallel ELM classifiers. In this article, 60 data samples are collected for each OPF and OSF. Considering 9 kinds of fault possibilities, a total of 540 data samples under the operations of 250, 500, and 750 r/min with and without load are acquired for the model training. The parameters

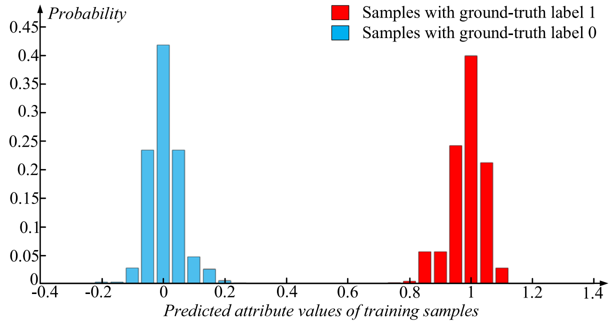

Fig. 8. Probability distribution histogram of predicted fault attributes.

of parallel ELM classifier only consist of the hidden node number $L$, the activation function $G$, and the hyperparameter $\alpha$. These parameters are usually determined by experience or violent search method. Since the scale of the parallel ELM classifier is relatively small, the hidden node number $L$ is set to 20 in this article. It has been studied that the sigmoid function is very suitable for the classification problem with better accuracy [28]. Thus, the sigmoid function is chosen as the activation function $G$ in this article. The small positive hyperparameter $\alpha$ is empirically selected as 0.02 in this article. The integrated attribute learner can be used for diagnosis after six parallel ELM classifiers are trained using (17). To reduce the online computational burden, the parallel ELM classifiers are enabled when the current tracking error on $d$–$q$ axis $\Delta I_{dq}$ becomes larger than the pre-set threshold. The fault occurrence indicator $\Delta I_{dq}$ is expressed as

$$\Delta I_{dq} = \sqrt{(i_d - i_d^*)^2 + (i_q - i_q^*)^2}. \tag{19}$$

By considering practical measurement and setting enough safety margin, the threshold of $\Delta I_{dq}$ is set to 0.3 A in this article. The selection of binarization threshold $f_{th}$ can be fulfilled by analyzing the patterns of predicted fault attributes in training data samples. The probability distribution histogram of predicted fault attributes in training data samples is shown in Fig. 8. It can be found from Fig. 8 that nearly all the predicted fault attribute values of training samples with ground-truth label 1 and 0 are above 0.8 and lower than 0.2, respectively. Considering both upper and lower boundaries, the binarization threshold $f_{th}$ is set to 0.5 in this article.

### B. Online Diagnosis

To verify the online applicability of the proposed method, real-time experiments are implemented in different operating states. To present the diagnostic results more clearly, a two-dimension look-up table is formed to indicate the occurrence of different OPFs and OSFs, as given in Table III. The fault location flag and fault category flag can jointly indicate the fault mode. Besides, the state flag is also presented in the experimental results to indicate whether the system remains normal state. It becomes 1 when a fault is detected and becomes 2 when the fault type is identified. The value 3 of state flag indicates that an unknown fault has been detected.

TABLE III
FLAGS OF DIAGNOSTIC RESULTS

| | | **Fault Category Flag** | | |
|---|---|---|---|---|
| | | 1 | 2 | 3 |
| **Fault Location Flag** | 1 | OPF-A | OSF-S$_{\mathrm{A1}}$ | OSF-S$_{\mathrm{A2}}$ |
| | 2 | OPF-B | OSF-S$_{\mathrm{B1}}$ | OSF-S$_{\mathrm{B2}}$ |
| | 3 | OPF-C | OSF-S$_{\mathrm{C1}}$ | OSF-S$_{\mathrm{C2}}$ |

In the experiment, both speed and load variations are considered to further verify the effectiveness of the proposed method. Fig. 9 shows the experimental diagnostic results of OPF-A under 100 r/min and no load. After the fault occurs, the phase-A current is forced to zero immediately, as shown in Fig. 9(a). In Fig. 9(b), the torque waveform in faulty operation shows the same pattern as the theoretical waveforms in Fig. 2(a), which verifies the correctness of the theoretical derivation in Section II-C. According to Fig. 9(b), the fault indicator $\Delta I_{dq}$ quickly exceeds its threshold after the fault occurs and the state flag changes from 0 to 1 at the same time, which indicates a fault has been detected. Then, the specific torque signals defined in Section III-A are collected as the network input within one fundamental period. In this way, the integrated attribute learner can output the fault attributes of the collected sample and the fault attribute vector is accordingly obtained after binarization. As shown in Fig. 9(c), both the fault location flag and fault category flag become 1. Thus, the OPF-A is determined based on Table III. Meanwhile, the state flag changes accordingly from 1 to 2, which indicates the completion of the diagnostic process. Fig. 10 shows the experimental diagnostic results of OPF-B under 600 r/min and 4.5 N·m load. After the fault classification process, the fault location flag and fault category flag in Fig. 10(c) becomes 2 and 1, respectively. According to Table III, the OPF-B is finally identified and the state flag turns into 2 accordingly.

Fig. 11 shows the experimental diagnostic results of OSF-S$_{\mathrm{A2}}$ under 100 r/min and no load. After the fault occurs, there is no negative component in phase-A current since $i_{\mathrm{A}}$ cannot inflow through the lower switch $S_{\mathrm{A2}}$, as shown in Fig. 11(a). The torque signal under faulty operation in Fig. 11(b) is consistent with the analysis in Section II-C. During the faulty half fundamental period, the torque waveform under OSF-S$_{\mathrm{A2}}$ follows the same pattern as the corresponding result under OPF-A in Fig. 9(b). By comparison, the output torque under OSF-S$_{\mathrm{A2}}$ becomes stable in the healthy half fundamental period, as shown in Fig. 11(b). The fault is detected instantly after the fault indicator $\Delta I_{dq}$ exceeds its threshold in Fig. 11(b). Then, the fault classification process is carried out and it takes less than one fundamental period to identify the specific fault. As shown in Fig. 11(c), the fault location flag and the fault category flag becomes 1 and 3, respectively. By searching the flags in Table III, the OSF-S$_{\mathrm{A2}}$ is finally identified. Fig. 12 shows the experimental diagnostic results of OSF-S$_{\mathrm{B1}}$ under 600 r/min and 4.5 N·m load. As shown in Fig. 12(b), the fault indicator $\Delta I_{dq}$ quickly exceeds its threshold, which indicates the fault occurrence. Then, it will take less than one fundamental period for the proposed method

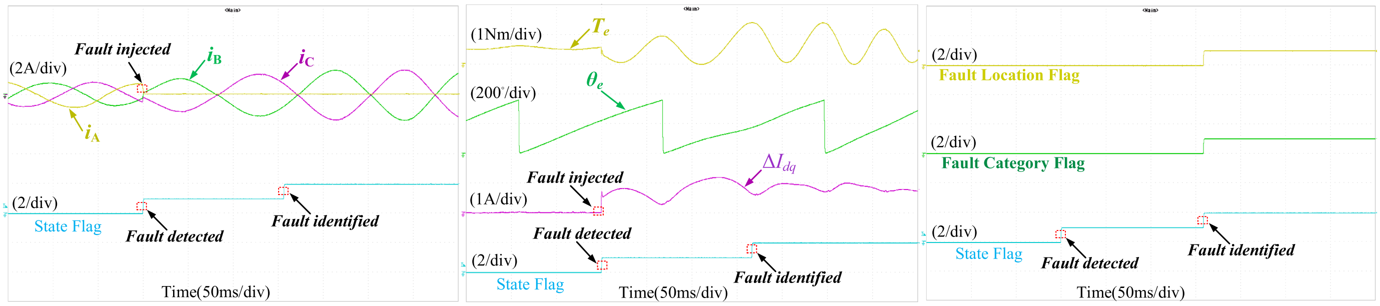

(a) (b) (c)

Fig. 9. Fault diagnosis of OPF-A under 100 r/min and no load. (a) Three-phase currents. (b) Diagnosis related signals. (c) Fault flags.

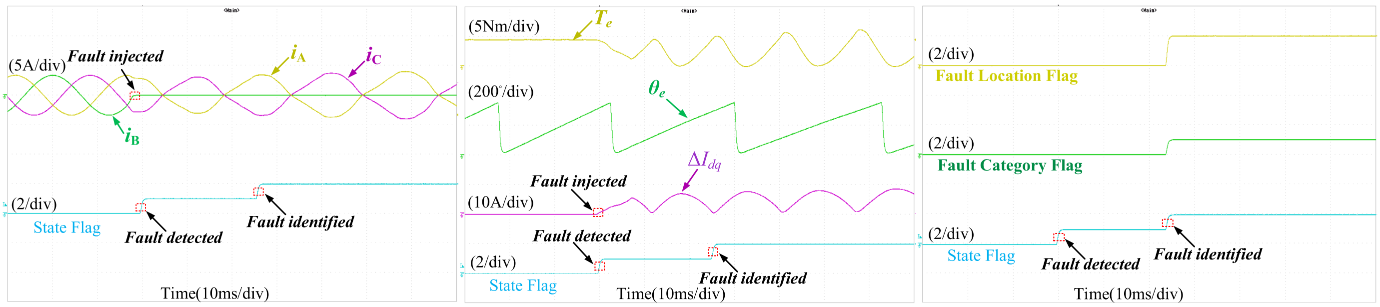

(a) (b) (c)

Fig. 10. Fault diagnosis of OPF-B under 600 r/min and 4.5 N·m load. (a) Three-phase currents. (b) Diagnosis related signals. (c) Fault flags.

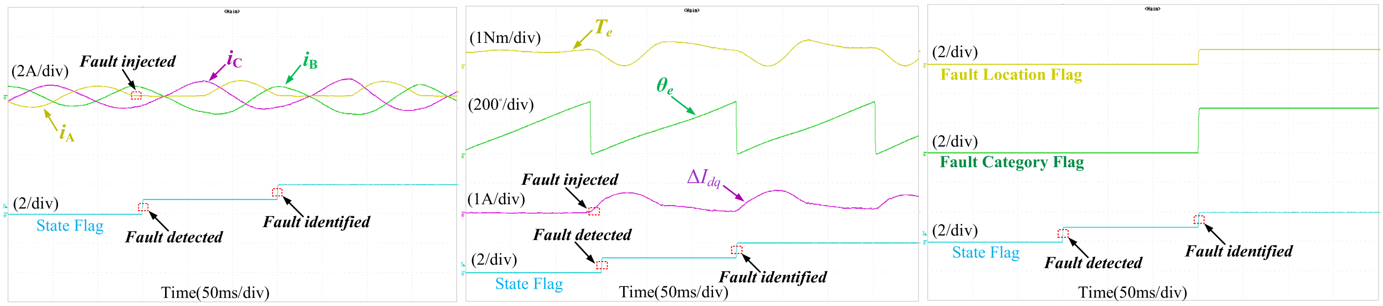

(a) (b) (c)

Fig. 11. Fault diagnosis of OSF-S$_{A2}$ under 100 r/min and no load. (a) Three-phase currents. (b) Diagnosis related signals. (c) Fault flags.

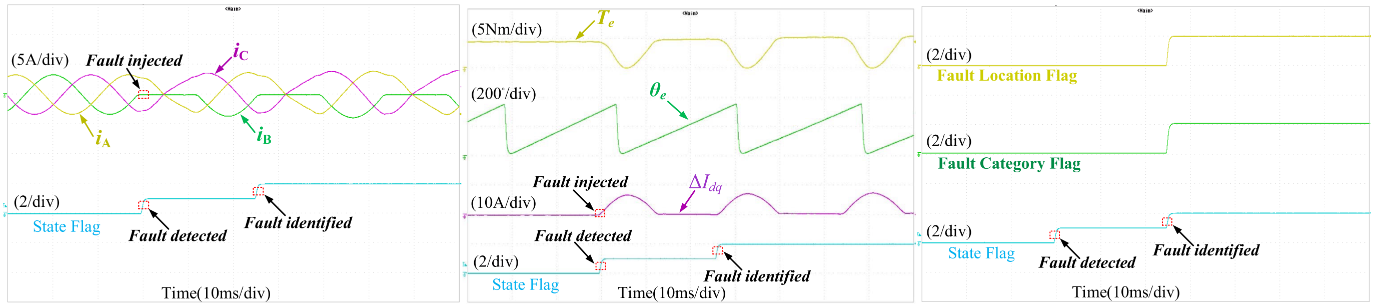

(a) (b) (c)

Fig. 12. Fault diagnosis of OSF-S$_{B1}$ under 600 r/min and 4.5 N·m load. (a) Three-phase currents. (b) Diagnosis related signals. (c) Fault flags.

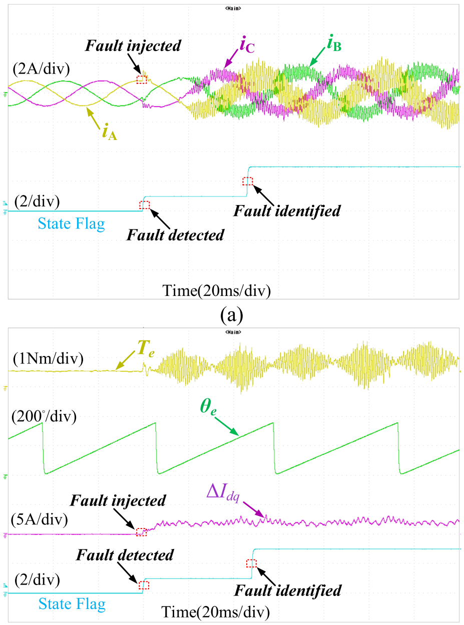

(a)

(b)

Fig. 13. Fault diagnosis of inter-turn short-circuit fault in phase-A under 300 r/min and no load. (a) Three-phase currents. (b) Diagnosis related signals.

to identify the specific fault. According to Fig. 12(c), both the fault location flag and fault category flag become 2. Thus, the OSF-$S_{B1}$ is identified based on Table III.

To verify the capability of the proposed method against misdiagnosis, Fig. 13 shows the experimental diagnostic results of inter-turn short-circuit (ITSC) fault in phase-A under 300 r/min and no load. The ITSC fault in phase-A is adopted as an unknown fault and it is simulated by externally connecting a small resistor between both ends of the phase-A winding. After the fault is introduced, the three-phase currents become abnormal, as shown in Fig. 13(a). The fault indicator $\Delta I_{dq}$ in Fig. 13(b) gradually increases and exceeds its threshold. Meanwhile, the state flag changes from 0 to 1, which indicates a fault has been detected. Then, the proposed method will predict the fault attributes of the present sample in less than one fundamental period. After the fault classification is finished, the predicted fault attribute vector does not match any target attribute vectors of candidate fault modes. Thus, the state flag changes from 1 to 3 and the ITSC fault in Phase-A is identified as an unknown fault successfully.

According to the experimental diagnosis results in Figs. 9(b)–12(b), the torque signals in the extracted features exhibit stable and unique waveforms under each fault mode, which is important for a robust data-driven diagnosis method. Since the proposed method can achieve accurate fault diagnosis with both speed and load variations in the experiments, the robustness of the proposed method is further justified. According to Figs. 9(c)–12(c), the fault attributes of present sample can be precisely determined with the selected optimal binarization threshold $f_{th}$. Instead of empirical determination, the optimal binarization threshold $f_{th}$ in the proposed method is obtained by fully utilizing the training samples, which also ensures the excellent diagnosis performance of the proposed method. In the aspect of fault diagnosis speed, the average computational time of the proposed method is 0.1ms after the data collection process is fulfilled, according to the online measurement results from DSP. The characteristic of low computational complexity enables the proposed method to be implemented online easily in the common industrial microcontrollers, guaranteeing the practicability of the proposed method. Regarding the verification of unknown fault indication, the experimental diagnosis results of Phase-A ITSC fault in Fig. 13 prove the effectiveness of the proposed attribute matching strategy against misdiagnosis. Obviously, the torque pattern of the occurred fault in Fig. 13(b) is not within the scope of candidate fault modes. Under this circumstance, the abnormal state of the motor drive will be indicated by the proposed method instead of selecting one of the candidate fault modes by mistake.

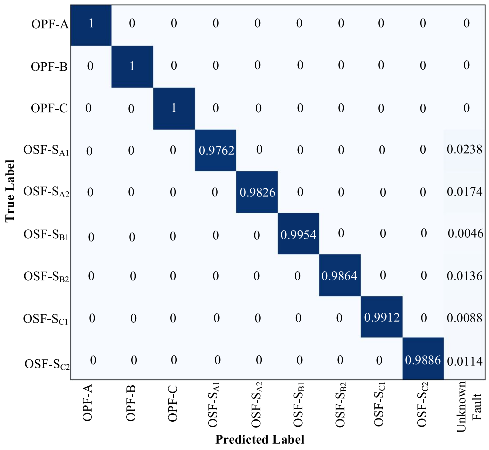

| | OPF-A | OPF-B | OPF-C | OSF-$S_{A1}$ | OSF-$S_{A2}$ | OSF-$S_{B1}$ | OSF-$S_{B2}$ | OSF-$S_{C1}$ | OSF-$S_{C2}$ | Unknown Fault |
|---|---|---|---|---|---|---|---|---|---|---|
| OPF-A | 1 | 0 | 0 | 0 | 0 | 0 | 0 | 0 | 0 | 0 |
| OPF-B | 0 | 1 | 0 | 0 | 0 | 0 | 0 | 0 | 0 | 0 |
| OPF-C | 0 | 0 | 1 | 0 | 0 | 0 | 0 | 0 | 0 | 0 |
| OSF-$S_{A1}$ | 0 | 0 | 0 | 0.9762 | 0 | 0 | 0 | 0 | 0 | 0.0238 |
| OSF-$S_{A2}$ | 0 | 0 | 0 | 0 | 0.9826 | 0 | 0 | 0 | 0 | 0.0174 |
| OSF-$S_{B1}$ | 0 | 0 | 0 | 0 | 0 | 0.9954 | 0 | 0 | 0 | 0.0046 |
| OSF-$S_{B2}$ | 0 | 0 | 0 | 0 | 0 | 0 | 0.9864 | 0 | 0 | 0.0136 |
| OSF-$S_{C1}$ | 0 | 0 | 0 | 0 | 0 | 0 | 0 | 0.9912 | 0 | 0.0088 |
| OSF-$S_{C2}$ | 0 | 0 | 0 | 0 | 0 | 0 | 0 | 0 | 0.9886 | 0.0114 |

Fig. 14. Confusion matrix of diagnostic results.

## C. Performance Evaluation and Comparison

In addition to the online experiments, the proposed method is further evaluated in the testing dataset to prove its good generalization performance. Different from the training dataset, the testing dataset which consists of 45 000 data samples (5000 for each fault mode) is collected under the operation states of 200, 400, and 600 r/min with and without load. The corresponding confusion matrix is presented in Fig. 14 to evaluate the diagnosis performance of the proposed method. As shown in Fig. 14, the proposed method can identify the OPF precisely and the average accuracy ranges from 97.62% to 99.54% for different OSFs under either speed variation or load variation, which proves the good generalization performance of the proposed method. Besides, it can be seen from Fig. 14 that the few mislabeled samples in OSF are all considered as unknown faults in the proposed method, which can avoid false alarms and improve the reliability of the proposed method.

To further validate the superiority of the proposed method over three state-of-the-art data-based fault diagnosis schemes [26], [9], [28], the comparison results of diagnostic accuracy and network complexity are shown in Fig. 15. For the convenience of comparison, the overall diagnostic accuracy of the proposed method is defined as the average value of the

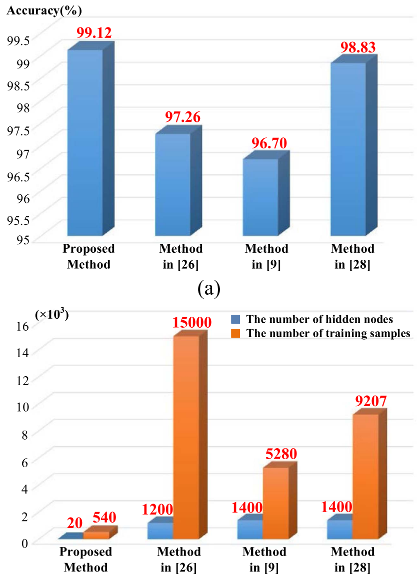

(a)

(b)

Fig. 15. Comparison results of performances between four different data-driven diagnosis methods. (a) Diagnostic accuracy. (b) Network complexity.

diagnostic accuracy in each fault mode and the network complexity is represented by both the number of hidden nodes and training data samples. Compared with three state-of-the-art data-based diagnosis methods for motor drives, the proposed method achieves the highest diagnostic accuracy of 99.12%, as shown in Fig. 15(a). In the aspect of network complexity, the proposed method can effectively identify each fault mode with only 20 hidden nodes and 540 training samples, as shown in Fig. 15(b). Compared with three state-of-the-art data-based diagnosis methods for motor drives, the required number of hidden nodes and training samples in the proposed method are significantly reduced, which directly promotes the decrease of computational complexity [37]. According to the comparison results in Fig. 15, the proposed few-sample data-driven diagnosis method can improve the diagnostic accuracy while reducing the computational complexity. Additionally, online verification results of the proposed method in the common industrial DSP microcontroller (TMS320F28335) have been presented to prove its online applicability, as shown from Figs. 9 to 13. During data collection process, 5/6 to one fundamental period are required in the proposed method to collect the extracted features, which is an essential process in the existing data-driven diagnosis methods for motor drives. Then, the proposed method can rapidly identify the specific fault mode within 0.1 ms, further indicating its lower computational complexity. In a word, the achievement of precise diagnosis with only few training data and lower computational burden makes the proposed method competitive and suitable for online data-driven fault diagnosis of motor drives in practical applications.

## V. CONCLUSION

In this article, an online attribute matching based data-driven diagnosis method is proposed for the OPF and OSF in PMSM drive. The extracted input features in the proposed method are theoretically proved to possess the stable patterns and distinguishable differences under different fault modes and can be easily obtained without consuming large computing resources. With the use of fault attributes, the proposed method can use smaller network size and fewer experimental data to identify each fault mode accurately, which ensures the practicality of the proposed method. Experimental results show that the proposed method can identify each fault mode including the unknown fault accurately within 0.1ms which only occupies 50% of one control period. Besides, it achieves an average diagnostic accuracy of 99.12% with lower computational complexity and few experimental data, which validates the effectiveness and practicality of the proposed method.

## REFERENCES

[1] A. Balamurali, G. Feng, A. Kundu, H. Dhulipati, and N. C. Kar, “Non-invasive and improved torque and efficiency calculation toward current advance angle determination for maximum efficiency control of PMSM,” *IEEE Trans. Transp. Electrific.*, vol. 6, no. 1, pp. 28–40, Mar. 2020.

[2] D. Xiao et al., “Universal full-speed sensorless control scheme for interior permanent magnet synchronous motors,” *IEEE Trans. Power Electron.*, vol. 36, no. 4, pp. 4723–4737, Apr. 2021.

[3] Z. Xia et al., “Computation-efficient online optimal tracking method for permanent magnet synchronous machine drives for MTPA and flux-weakening operations,” *IEEE J. Emerg. Sel. Topics Power Electron.*, vol. 9, no. 5, pp. 5341–5353, Oct. 2021.

[4] J. Hang, H. Wu, S. Ding, Y. Huang, and W. Hua, “Improved loss minimization control for IPMSM using equivalent conversion method,” *IEEE Trans. Power Electron.*, vol. 36, no. 2, pp. 1931–1940, Feb. 2021.

[5] L. Jin, Y. Mao, X. Wang, P. Shi, L. Lu, and Z. Wang, “Optimization-based maximum-torque fault-tolerant control of dual three-phase PMSM drives under open-phase fault,” *IEEE Trans. Power Electron.*, vol. 38, no. 3, pp. 3653–3663, Mar. 2023.

[6] P. Shi, X. Wang, X. Meng, M. He, Y. Mao, and Z. Wang, “Adaptive fault-tolerant control for open-circuit faults in dual three-phase PMSM drives,” *IEEE Trans. Power Electron.*, vol. 38, no. 3, pp. 3676–3688, Mar. 2023.

[7] C. Gan, X. Li, Z. Yu, K. Ni, S. Wang, and R. Qu, “Modular seven-leg switched reluctance motor drive with flexible winding configuration and fault-tolerant capability,” *IEEE Trans. Transp. Electrific.*, vol. 9, no. 2, pp. 2711–2722, Jun. 2023.

[8] Y. Zhang, Y. Mao, X. Wang, Z. Wang, D. Xiao, and G. Fang, “Current prediction-based fast diagnosis of electrical faults in PMSM drives,” *IEEE Trans. Transp. Electrific.*, vol. 8, no. 4, pp. 4622–4632, Dec. 2022.

[9] Y. Xia, Y. Xu, and B. Gou, “A data-driven method for IGBT open-circuit fault diagnosis based on hybrid ensemble learning and sliding-window classification,” *IEEE Trans. Ind. Inform.*, vol. 16, no. 8, pp. 5223–5233, Aug. 2020.

[10] Q. T. An, L. Sun, and L.-Z. Sun, “Current residual vector-based open-switch fault diagnosis of inverters in PMSM drive systems,” *IEEE Trans. Power Electron.*, vol. 30, no. 5, pp. 2814–2827, May 2015.

[11] W. Huang, J. Du, W. Hua, K. Bi, and Q. Fan, “A hybrid model-based diagnosis approach for open-switch faults in PMSM drives,” *IEEE Trans. Power Electron.*, vol. 37, no. 4, pp. 3728–3732, Apr. 2022.

[12] J. Hang, H. Wu, J. Zhang, S. Ding, Y. Huang, and W. Hua, “Cost function-based open-phase fault diagnosis for PMSM drive system with model predictive current control,” *IEEE Trans. Power Electron.*, vol. 36, no. 3, pp. 2574–2583, Mar. 2021.

[13] S. Zhuo, A. Gaillard, L. Xu, C. Liu, D. Paire, and F. Gao, “An observer-based switch open-circuit fault diagnosis of DC–DC converter for fuel cell application,” *IEEE Trans. Ind. Appl.*, vol. 56, no. 3, pp. 3159–3167, May/Jun. 2020.

[14] D. U. Campos-Delgado and D. R. Espinoza-Trejo, “An observer-based diagnosis scheme for single and simultaneous open-switch faults in induction motor drives,” *IEEE Trans. Ind. Electron.*, vol. 58, no. 2, pp. 671–679, Feb. 2011.

[15] N. Wassinger, E. Penovi, R. G. Retegui, and S. Maestri, “Open-circuit fault identification method for interleaved converters based on time-domain analysis of the state observer residual,” *IEEE Trans. Power Electron.*, vol. 34, no. 4, pp. 3740–3749, Apr. 2019.

[16] D. Xie and X. Ge, "A state estimator-based approach for open-circuit fault diagnosis in single-phase cascaded H-bridge rectifiers," *IEEE Trans. Ind. Appl.*, vol. 55, no. 2, pp. 1608–1618, Mar./Apr. 2019.

[17] B. Li, S. Shi, B. Wang, G. Wang, W. Wang, and D. Xu, "Fault diagnosis and tolerant control of single IGBT open-circuit failure in modular multilevel converters," *IEEE Trans. Power Electron.*, vol. 31, no. 4, pp. 3165–3176, Apr. 2016.

[18] J. Poon, P. Jain, C. Spanos, S. K. Panda, and S. R. Sanders, "Fault prognosis for power electronics systems using adaptive parameter identification," *IEEE Trans. Ind. Appl.*, vol. 53, no. 3, pp. 2862–2870, May/Jun. 2017.

[19] W. Sleszynski, J. Nieznanski, and A. Cichowski, "Open-transistor fault diagnostics in voltage-source inverters by analyzing the load currents," *IEEE Trans. Ind. Electron.*, vol. 56, no. 11, pp. 4681–4688, Nov. 2009.

[20] W. Huang et al., "Current-based open-circuit fault diagnosis for PMSM drives with model predictive control," *IEEE Trans. Power Electron.*, vol. 36, no. 9, pp. 10695–10704, Sep. 2021.

[21] J. O. Estima and A. J. Marques Cardoso, "A new algorithm for real-time multiple open-circuit fault diagnosis in voltage-fed PWM motor drives by the reference current errors," *IEEE Trans. Ind. Electron.*, vol. 60, no. 8, pp. 3496–3505, Aug. 2013.

[22] J. Zhang, X. Hu, S. Xu, Y. Zhang, and Z. Chen, "Fault diagnosis and monitoring of modular multilevel converter with fast response of voltage sensors," *IEEE Trans. Ind. Electron.*, vol. 67, no. 6, pp. 5071–5080, Jun. 2020.

[23] M. A. Rodriguez-Blanco et al., "A failure-detection strategy for IGBT based on gate-voltage behavior applied to a motor drive system," *IEEE Trans. Ind. Electron.*, vol. 58, no. 5, pp. 1625–1633, May 2011.

[24] J. Hang, J. Zhang, M. Cheng, and S. Ding, "Detection and discrimination of open-phase fault in permanent magnet synchronous motor drive system," *IEEE Trans. Power Electron.*, vol. 31, no. 7, pp. 4697–4709, Jul. 2016.

[25] W. Lang, Y. Hu, C. Gong, X. Zhang, H. Xu, and J. Deng, "Artificial intelligence-based technique for fault detection and diagnosis of EV motors: A review," *IEEE Trans. Transp. Electrific.*, vol. 8, no. 1, pp. 384–406, Mar. 2022.

[26] T. Wang, H. Xu, J. Han, E. Elbouchikhi, and M. E. H. Benbouzid, "Cascaded H-bridge multilevel inverter system fault diagnosis using a PCA and multiclass relevance vector machine approach," *IEEE Trans. Power Electron.*, vol. 30, no. 12, pp. 7006–7018, Dec. 2015.

[27] B. Cai, Y. Zhao, H. Liu, and M. Xie, "A data-driven fault diagnosis methodology in three-phase inverters for PMSM drive systems," *IEEE Trans. Power Electron.*, vol. 32, no. 7, pp. 5590–5600, Jul. 2017.

[28] B. Gou, Y. Xu, Y. Xia, Q. Deng, and X. Ge, "An online data-driven method for simultaneous diagnosis of IGBT and current sensor fault of three-phase PWM inverter in induction motor drives," *IEEE Trans. Power Electron.*, vol. 35, no. 12, pp. 13281–13294, Dec. 2020.

[29] G. B. Huang, Q. Y. Zhu, and C. K. Siew, "Extreme learning machine: Theory and applications," *Neurocomputing*, vol. 70, no. 1–3, pp. 489–501, May 2006.

[30] X. Wang, Z. Wang, M. He, Q. Zhou, X. Liu, and X. Meng, "Fault-tolerant control of dual three-phase PMSM drives with minimized copper loss," *IEEE Trans. Power Electron.*, vol. 36, no. 11, pp. 12938–12953, Nov. 2021.

[31] M. Sun, H. Wang, P. Liu, Z. Long, J. Yang, and S. Huang, "A novel data-driven mechanical fault diagnosis method for induction motors using stator current signals," *IEEE Trans. Transp. Electrific.*, vol. 9, no. 1, pp. 347–358, Mar. 2023.

[32] G. B. Huang and L. Chen, "Enhanced random search based incremental extreme learning machine," *Neurocomputing*, vol. 71, no. 16–18, pp. 3460–3468, Oct. 2008.

[33] J.-M. Huang, R.-J. Wai, and G.-J. Yang, "Design of hybrid artificial bee colony algorithm and semi-supervised extreme learning machine for PV fault diagnoses by considering dust impact," *IEEE Trans. Power Electron.*, vol. 35, no. 7, pp. 7086–7099, Jul. 2020.

[34] Z. Chen, C. Jiang, and L. Xie, "A novel ensemble ELM for human activity recognition using smartphone sensors," *IEEE Trans. Ind. Inform.*, vol. 15, no. 5, pp. 2691–2699, May 2019.

[35] C. Deng, Y. Han, and B. Zhao, "High-performance visual tracking with extreme learning machine framework," *IEEE Trans. Cybern.*, vol. 50, no. 6, pp. 2781–2792, Jun. 2020.

[36] Z. Deng, K.-S. Choi, Y. Jiang, and S. Wang, "Generalized hidden-mapping ridge regression, knowledge-leveraged inductive transfer learning for neural networks, fuzzy systems and kernel methods," *IEEE Trans. Cybern.*, vol. 44, no. 12, pp. 2585–2599, Dec. 2014.

[37] H. Cheng, Y. Xia, Y. Huang, Z. Lu, and L. Yang, "Deep neural network aided low-complexity MPA receivers for uplink SCMA systems," *IEEE Trans. Veh. Technol.*, vol. 70, no. 9, pp. 9050–9062, Sep. 2021.

**Luhan Jin** (Graduate Student Member, IEEE) received the B.S. degree in communication engineering from Zhengzhou university, Zhengzhou, China, in 2021. He is currently working toward the Ph.D. degree in measuring technology and instrument with the Institute of Optics and Electronics, Chinese Academy of Science, Beijing, China.

His current research interests include the fault diagnosis and tolerant control of motor drives and distributed multi-agent system, digital twin modeling and control optimization of motor drives.

**Xueqing Wang** (Member, IEEE) received the B.S. degree from Tianjin University of Science and Technology, Tianjin, China, in 2014, and the M.S. and Ph.D. degrees from Southeast University, Nanjing, China, in 2016 and 2020, respectively, all in electrical engineering.

From 2018 to 2019, he was a joint Ph.D. with McMaster Automotive Resource Centre, McMaster University, Hamilton, Canada. He is currently an Associate Research Fellow with the College of Electrical Engineering, Sichuan University, Chengdu, China. His research interests include control of multiphase motor and open-winding motor, fault diagnosis and tolerant control of motor drive, multilevel PWM strategy.

**Yao Mao** (Member, IEEE) received the B.S. degree in automatic control from the Department of Automation, Chongqing University, Chongqing, China, in 2001, and the Ph.D. degree in signal and information processing from the Institute of Optics and Electronics, Chinese Academy of Science, Beijing, China, in 2012.

Since 2016, he has been a Professor with the University of Chinese Academy of Sciences, Beijing, China. His research interests include power electronics, motion control, information fusion, machine learning.

Dr. Mao was the recipient of Distinguished Scientific Achievement Award by the Chinese Academy of Science in 2011.

**Linlin Lu** (Student Member, IEEE) received the B.E. degree in communication engineering from Zhengzhou University, Zhengzhou, China, in 2021. She is currently working toward the M.S. degree in measuring technology and instrument with the Institute of Optics and Electronics, Chinese Academy of Science, Beijing, China.

Her current research interests include the optimal control of permanent magnet motors.

**Zheng Wang** (Senior Member, IEEE) received the B.Eng. and M.Eng. degrees from Southeast University, Nanjing, China, in 2000 and 2003, respectively, and the Ph.D. degree from The University of Hong Kong, Hong Kong, in 2008, all in electrical engineering.

From 2008 to 2009, he was a Postdoctoral Fellow with Ryerson University, Toronto, ON, Canada. He is currently a full Professor with the School of Electrical Engineering, Southeast University, China. He has authored or coauthored more than 80 internationally refereed papers and four books in these areas. His research interests include electric drives, power electronics, and distributed generation.

Dr. Wang received several academic awards including IEEE PES Chapter Outstanding Engineer Award and Best Paper Award of International Conference on Electrical Machines and Systems.